

Induced Birefringence in 3D Printing: Concealing Information Optically within Printed Objects

David Michael Roper,* Kyung-Ah Kwon, Luke Peter Malone, Serena Michelle Best, and Ruth Elizabeth Cameron*

This paper presents a novel method to spatially vary the intra-layer birefringence of Fused Filament Fabricated (FFF) parts by controlling chain alignment during extrusion along individual rasters. The role of print speed, extrusion factor and layer separation on the birefringence of single PLLA layers is explored, at thicknesses ranging from 50–125 μm and print speeds 1000–6000 mm min^{-1} . The cumulative and subtractive effect of multiple PLLA layers are explored to elicit colours corresponding to a range of retardations, achieve complete extinction, and printing a physical Michel-Levy chart. By increasing print speed and reducing layer separation and extrusion factor, a birefringence up to $\Delta n = 9 \times 10^{-4}$ could be achieved in single layers. In multi-layer structures, retardations of 0–800 nm are demonstrated. These results suggest that spatially varied birefringence can be used to store data, text or images, which can be resolved when parts are illuminated between polarizers. This effect is utilized to present a steganographic technique embedding information within bulk printed parts. These techniques might find application in a range of printed optics and devices, where spatial control over molecular alignment and associated influence on the propagation of light is desirable, including the ability to encode information within a print.

1. Introduction

Additive manufacturing techniques, such as fused filament fabrication (FFF), Stereolithography (SLA) and Multiphoton lithography, present new opportunities to implement well known material phenomena into a wide range of devices. The use of shape memory polymers in stereolithographic and extrusion based 3D printing allows the production of actuating architectures such as flexible electronics^[1] and self-folding parts^[2–5] stimulated by temperature changes. 3D printing material development has allowed innovation in the production of structures

capable of properties at extremes ranging from light emission^[6–8] to tailoring degradation and drug release.^[9–12] The 3D printing of optics is also a rapidly progressing and emerging field, with the potential to allow not only the design of new photonic structures, but also embed optics within parts to form functional interactive devices.^[13] Stereolithographic printing can be combined with surface finishing techniques utilized to print complex reflective surfaces for optical components.^[14] Multiphoton lithography has allowed the direct writing of optics ranging from micro lenses and mirrors^[14] to high resolution waveguides.^[15] The refractive index of micro optics can also be varied through the incorporation of nanocomposites,^[16] and tunable photonics generated through the use of photoresponsive polymers.^[17] Whilst work on extrusion based 3D printed photonics is less developed, extruded waveguides allow the formation of soft, stretchable optics^[18] that

might be formed using biodegradable materials.^[19] This may be useful in rapid development of patient specific treatment for deep tissue photostimulation.^[20]

The alignment and straightening of molecular chains during the extrusion of polymers is a commonly understood phenomenon. To some extent, alignment has also been shown within extrusion based 3D printing. For example, Ghodbane et al. demonstrate molecular orientation within printed poly(desaminotyrosyl-tyrosine dodecyl dodecanedioate), poly(DTD DD), deposited using pneumatically driven extrusion.^[21] However, this reported alignment is essentially a geometric variation on conventional melt drawing. Under a constant deposition pressure, increasing translational speed leads to an increased draw ratio, which is accommodated through molecular alignment. The drawing of material is also discussed by Udofia and Zhou in the context of pneumatically driven microextrusion^[22] as an extension of fluid dragging on translating surfaces.^[23] Here, there is an ambiguity in the description of 3D printing parameters. In the work of Ghodbane et al.,^[21] translational speed and extrusion are not linked—increasing print speed results in an effectively reduced deposition at a given point within a print. Any control over the alignment generated therefore results in a change of shape in the deposited material, and severally restricts property variation during printing.

D. M. Roper, K. A. Kwon, L. P. Malone, S. M. Best, R. E. Cameron
Department of Materials Science and Metallurgy
University of Cambridge
27 Charles Babbage Road, Cambridge CB3 0FS, UK
E-mail: dmr53@cam.ac.uk; rec11@cam.ac.uk

 The ORCID identification number(s) for the author(s) of this article can be found under <https://doi.org/10.1002/admt.202200139>.

© 2022 The Authors. Advanced Materials Technologies published by Wiley-VCH GmbH. This is an open access article under the terms of the Creative Commons Attribution License, which permits use, distribution and reproduction in any medium, provided the original work is properly cited.

DOI: 10.1002/admt.202200139

Recently, Hassan et al. have measured the effects of shear induced alignment on both freely extruded polycarbonate and structures deposited during 3D printing using Raman spectroscopy and birefringence.^[24] This provided the first measurement of birefringence in extrusion based 3D printing. This analysis however negates the deformation of the melt between the nozzle and print surface, and focuses instead on establishing a relationship between alignment measured through Raman spectroscopy and birefringent compensation. Alignment achieved through shear in the nozzle represents a fraction of the potential orientation achieved through forces exerted through drawing by the translation of the print surface as observed and reported by Ghodbane et al.^[21]

Several questions remain in understanding the alignment induced during 3D printing. Firstly, the degree to which printing parameters influence molecular alignment and the associated interaction between light and the deposited material has yet to be established. It may be asked whether the increased alignment during printing originates from the increased rate of deformation defined by the rate of strain due to the relative motion between the nozzle and the print surface, or from the higher overall strain achieved in the deformation (as material is stretched over greater volumes if extrusion and print speed are not linked).

In this paper, we show for the first time spatially varying alignment within 3D printed layers. Deposition is controlled by an extrusion factor, which fixes the amount of material ejected by a print head (measured by the length of filament extruded) to the distance travelled by the print head across the printing surface.^[25] In this way, variations in molecular alignment can be achieved without altering deposition dimensions. The alignment demonstrated here contrasts with that previously reported as it constitutes a transition in the accommodation of strain during deposition. That is, at a fixed extrusion factor, increasing printing speed results in an increased strain rate. This promotes a controllable transition by altering the deformation conditions of the extrudate as it is deposited within a 3D printed layer. In this way, alignment can be varied along a printed layer without changing the amount of material deposited. This, to our knowledge, is the first demonstration of within layer varying material properties during 3D printing.

As 3D printers offer point-by-point polymer processing, they present an opportunity to locally tailor material properties to interact with light. In this work, we demonstrate an induced birefringence during 3D printing. We present a simple model for the controlled induction birefringence driven by strain rate, dependent on nozzle and filament diameters, print speed and an extrusion factor. Birefringence can be calculated by dividing an observed retardation (the optical path difference between a fast and slow axis within a material) by the sample thickness. The retardation of single layer PLLA was measured using an Ehringhaus compensator for a range of print speeds and programmed layer separations. Further, multilayer structures were printed to show the cumulative effect on sample retardation of increasing layer number. Further we demonstrate extinction by utilizing perpendicular printing directions. These concepts are combined to 3D print a physical Michel-Levy chart.

These developments in spatially varying birefringence demonstrated were finally utilized to produce steganographic 3D prints. Steganography refers to the process of concealing information within an object, an as of yet under-explored area of 3D printing. The information concealed could for example be

identification details which would allow part tracking or enable authenticity variation. Current attempts which demonstrate steganography during 3D printing necessitate the altering of a 3D printed structure to encode this information, by either using different materials, omitting printing regions or selectively offsetting layers.^[25–27] These techniques are not optimal, as variations through negative space, offsets or material changes weaken the printed structure with voids and compromising inter-layer bonding. Alternatively, the optical properties of printed material can be harnessed to manipulate light to reveal data. For example, D'Elia et al. use refraction through printed features to create projections, and molds to fabricate transparent cryptographic windows, which reveal scannable QR codes when stretched.^[26] Ideally, however steganographic printing without geometrically altering a surface is desirable. Here, by utilizing variations in induced birefringence, information can instead be encoded within 3D prints without altering their physical structure. To demonstrate this effect, we conceal a two colour logo, and a five colour cartoon character, which can be revealed when viewed between crossed polarizing filters.

2. Modeling Induced Birefringence

The deformation of polymer melt as it exits a nozzle, makes contact with the printing surface, and is strained by the relative motion of the nozzle has the potential to drive molecular orientation and alignment through the extension of polymer chains. Here, we implement a model based on extensional flow as a simplification of the complex interaction taking place during deposition. The variables used in discussing FFF printing in this paper are listed in **Table 1**. Derivation of this model is provided in the supplementary material and serves as a rough guide to contextualise and simplify the complex melt dynamics taking place driven by extrusion during 3D printing. The key results of this model are summarized here where relevant.

The understanding of the implications of the model are aided through the idealized schematic shown in **Figure 1a**, representing the extrusion of material from a nozzle during the deposition the “*n*th” layer of a multilayer print. In this scenario, the nozzle is at a stand-off distance $L + \psi$ from the surface of the preceding layer. This includes the layer separation L , and an offset, ψ , to account for both any original miscalibration (an unknown initial stand-off distance) and the cumulative effect of variable layer thicknesses of each of the previous layers prior to the establishment of stable printing (as discussed in the supplementary material). **Figure 1b** shows the deposition of a

Table 1. Symbol definitions used to describe 3D printing.

a	Filament Diameter (mm)
b	Nozzle Diameter (mm)
ν_f	Feed rate (mm min ⁻¹)
ν_m	Exit Speed (mm min ⁻¹)
ν_p	Print Speed (mm min ⁻¹)
L	Layer separation (mm)
ψ	Offset (mm)
h	Layer Thickness (mm)

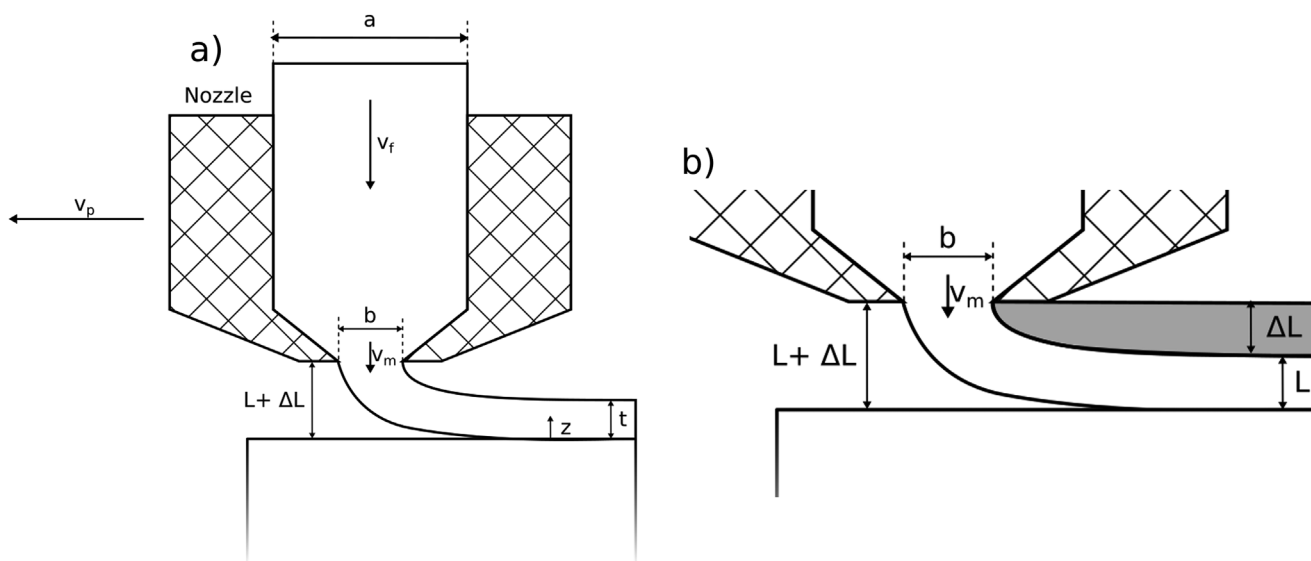


Figure 1. a) A schematic showing the printing of the “*n*th” layer of a multilayer print, where a filament of material (diameter = *a*, feed rate = v_f) is extruded from a nozzle (diameter = *b*) moving relative to a print bed at a velocity v_p . The nozzle is raised above the print surface by a programmed layer separation, *L*, plus an additional offset ψ . Material is shown to exit the nozzle at a velocity v_m . This results in the deposition of a layer of thickness *h*, with the height of an element within the layer represented by the variable *z*. b) A close up on the printing of a layer under the stable printing condition such that programmed layer separation is equivalent to layer thickness, $L = h$. A volume of interest bounded by a thickness ψ is shaded grey.

layer under the stable printing condition, programmed layer separation = layer thickness, $L = h$.

The model centers on the visualization of the deformation of an element of material as it exits the nozzle, is drawn by the relative motion between the nozzle and the print surface, and reaches rest. During this time, a strain, ϵ , is experienced by the element throughout the time taken to reach the print bed, *t*, such that

$$\epsilon = \frac{\Delta vt}{v_m t} = \frac{b^2}{ea^2} - 1 \quad (1)$$

Where the extrusion factor, *e*, ensures volume of extruded material is conserved across all print speeds^[25]

$$e = \text{length of filament extruded/horizontal nozzle displacement} \quad (2)$$

Polymer printed for the condition $e < \frac{b^2}{a^2}$ is effectively under extruded. For a nozzle and filament diameter of 400 μm and 1.75 mm respectively this condition is $e < 0.052$.

The accommodation of strain during print can be considered with respect to the relaxation of molecular chains, such that the response of the polymer melt will exhibit viscoelastic properties, where its material response is dependent on both the magnitude and rate of deformation.^[27] In thermoplastic polymers, at sufficiently high temperatures where chains have sufficient thermal energy to overcome intermolecular and mutual entanglement, polymers experience molten flow. In this state, strain can be accommodated by either the relative motion between molecular chains (chain sliding with respect to one another), or the extension of chains through changes in conformation. Molecular chains offer a resistance to extension through a preference toward disordered conformation states, behaving as “entropic springs”^[28] and relax to a more disordered state once

an applied stress is removed. Alignment can be maintained if the polymer is cooled below its glass transition temperature, T_g , on a faster timescale than its chain relaxation.

Intermolecular motion and conformational state changes operate on different timescales. If the elongation of the melt is slow, chains may have sufficient time to slide with respect to one another and relax, such that on a molecular scale the deformed melt is indistinguishable from the undeformed. If elongation is rapid and exceeds the relaxation time of polymer chains, it must be accommodated by conformational changes, chain alignment and potentially lead to a degree of strain induced crystallisation. The transition between these mechanisms might be related to the strain rate of material within the element, which sets the timescale of the deformation.^[27,29–32] This alignment might be facilitated by either shear or extensional flow, and in most situations is likely to be a combination of both. Here, the flow and strain rate experienced is modeled as an extensional flow.

To accommodate the promotion of both the chain alignment and entropic relaxation during printing, induced retardation, Γ , was modelled as the solution to a first order differential equation of the form

$$\Gamma = \Gamma_{\max} (1 - \exp(-\Omega)) \quad (3)$$

Through consideration of the strain rate experienced by an element of material during deformation as a plausible Ω , is suggested such that

$$\Gamma = \Gamma_{\max} \left(1 - \exp \left(-B \frac{v_p}{2} \left(\frac{b^2}{ea^2} - \frac{ea^2}{b^2} \right) \ln \left(\frac{2}{\epsilon} \right) \right) \right) \quad (4)$$

where *B* is a constant of proportionality.

A series of predictions might be verified experimentally:

- There is a measurable induced birefringence due to the relative motion between the nozzle and print surface during deposition (in addition to any alignment induced through shear within the nozzle during extrusion).
- Induced birefringence varies with extrusion factor and print speed. For maximum induced birefringence, layers should be printed at high speed with both the layer separation and extrusion factor minimized.
- Under the stable printing condition, induced retardation is independent of layer separation.
- Induced retardation takes the form $\Gamma = \Gamma_{\max} (1 - \exp(-\Omega))$, where B is a constant for factors such as the specific material (e.g., molecular weight, viscosity), extrusion and print surface temperatures, T_{ext} and T_{bed} .

3. Results and Discussion

3.1. Induced Birefringence in Single layers

To explore the effect of layer separation and print speed on induced birefringence in 3D printed PLLA, layers were deposited at a constant extrusion factor. The modeled expression for induced birefringence introduced previously shows heavy dependence on the extrusion factor selected for printing. Here, we select a low extrusion factor, $e_{\text{PLLA}} = 0.01$, to print PLLA layers with a high expected birefringence whilst maintaining continuous printing across a range of reasonable layer separations. In this way, samples are thick enough to produce retardations (20–40 nm) measurable to sufficient accuracy (± 3 nm). Single PLLA layers were printed on a PVA support layer detailed in our previous work.^[25] Figure 2 shows the measured birefringence of single PLLA layers for a range of programmed layer separations ($L_{\text{PLLA}} = 50, 75, 100,$ and $125 \mu\text{m}$) deposited at an extrusion factor $e_{\text{PLLA}} = 0.01$ and print speeds $v_p = 1000, 2000,$

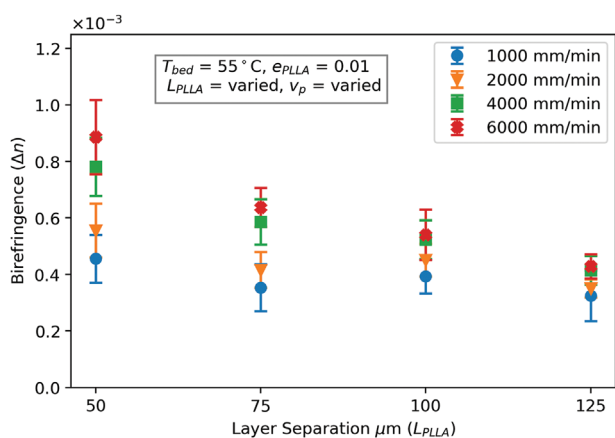


Figure 2. A plot showing the variation of measured birefringence, Δn , of single PLLA layers with programmed layer separation, $L_{\text{PLLA}} = 50$ – $125 \mu\text{m}$, and print speed, $v_p = 1000$ – 6000 mm min^{-1} at an extrusion factor $e_{\text{PLLA}} = 0.01$. Average layer thicknesses, h_{PLLA} , were measured as $h_{\text{PLLA}} = 48 \pm 5, 53 \pm 6, 72 \pm 6,$ and $90 \pm 10 \mu\text{m}$ for layer separations $L_{\text{PLLA}} = 50$ – $125 \mu\text{m}$ respectively.

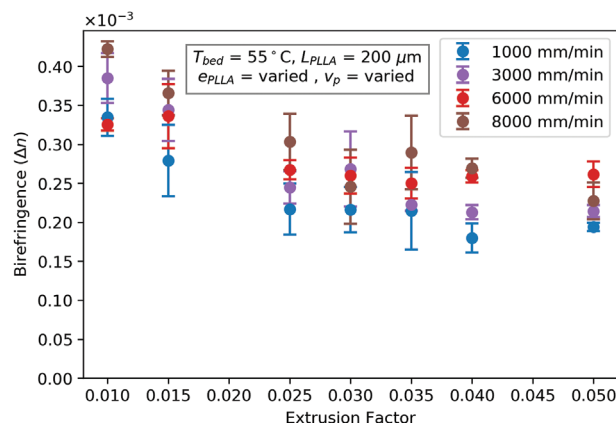


Figure 3. A plot showing the variation of measured birefringence, Δn , of single PLLA layers with programmed layer separation, $L_{\text{PLLA}} = 200 \mu\text{m}$, and print speed, $v_p = 1000$ – 8000 mm min^{-1} for extrusion factors $e_{\text{PLLA}} = 0.01$ – 0.05 . Average layer thicknesses, h_{PLLA} , were measured as $h_{\text{PLLA}} = 113 \pm 13, 116 \pm 13, 112 \pm 9, 128 \pm 19, 143 \pm 28, 138 \pm 10,$ and $151 \pm 5 \mu\text{m}$ for extrusion factors $e_{\text{PLLA}} = 0.01$ – $0.05 \mu\text{m}$ respectively.

4000, and 6000 mm min^{-1} . Birefringence is shown to increase with print speed across all layer separations. This dependency is more pronounced at lower layer separations, with the difference between Δn at $v_p = 1000$ and 6000 mm min^{-1} decreasing with increasing layer separation, L_{PLLA} .

To observe the effect of extrusion factor on the induced birefringence within 3D printed PLLA, single PLLA layers were printed at a fixed layer separation. Figure 3 shows the measured birefringence of single PLLA layers for a range of extrusion factors $e_{\text{PLLA}} = 0.01$ – 0.05 , for print speeds $v_p = 1000, 3000, 6000,$ and 8000 mm min^{-1} , deposited at a layer separation $L_{\text{PLLA}} = 200 \mu\text{m}$. These results represent a continuation of those presented in Figure 2, as the value for $e_{\text{PLLA}} = 0.01$ on this figure continues the trend observed previously. There is minimal to no statistical difference in induced birefringence with print speed observed in this figure. It could be said that layers printed at faster speeds tend to have a higher birefringence than those printed at lower speed, but experimental error represents a significant fraction of the absolute value measured. Birefringence is shown to increase with decreasing extrusion factor, and is the highest ($\Delta n = 0.425 \times 10^{-3}$) at the maximum speed and lowest extrusion factor ($e_{\text{PLLA}} = 0.01$) presented in Figure 3.

The results of Figures 2 and 3 are significant in demonstrating alignment within 3D printed PLLA, which Ghodbane et al. previously suggested might not be possible due to the short window of time available to shear and align chains, and preserve orientation on cooling.^[21] The results of this figure suggest low layer separation and high printing speed are necessary to promote alignment. They also present an insight into the lack of previous reporting of control over birefringence in 3D printing. Firstly, an e_{PLLA} of 0.01 represents a highly underextruded print, where typically 3D printed parts are likely prepared at closer to ideal or over extrusion. A highly underextruded print provides sufficient strain which must be accommodated by chain alignment. In Figure 3, higher values of extrusion factor induce a significantly smaller birefringence. Secondly, the birefringence values measured are low and require multiple layers to achieve a visible effect on the transmission of

light. The required printing speeds, in the range of thousands of millimetres per minute are quite high for an average printed part. Thirdly, the disconnect between extrusion feed rates and transverse printing speeds (addressed by the introduction of an extrusion factor previously^[25]) have made distinguishing the influence of parameters on part properties difficult. Fourthly, the difference in induced birefringence is only clearly distinguished at lower layer separations, owing to an increased strain rate during deposition. A typical 3D print is likely printed at a programmed layer separation of 200 μm on average, 100 μm at best, which may be too high to observe sufficient alignment. Finally, observation of induced birefringence necessitates the need for transparent filament, where more common printing materials contain colored fillers and are opaque.

The derived Equation S1 in the Supporting Information suggests that for a nozzle and filament diameter of 400 μm and 1.75 mm respectively, material deposited at $e = 0.052$ should not present as birefringent. However, Figure 3 shows measurable birefringence at $e = 0.05$. This observed birefringence may be due to either shear within the nozzle, or alignment imparted during spreading across the print surface during deposition. Likewise, considering the trend observed in Figure 2, which highlights a decaying birefringence with increasing layer separation, as $L_{\text{PLLA}} \Rightarrow \infty$ it might be expected that this value reach zero, such that no birefringence is increased within the samples. Again, this neglects the orientation that might be imparted due to the shear stress within the nozzle that is experienced as material is extruded during deposition. The birefringence of material in free-extrusion from a 3D printer nozzle has been characterised previously by Hassan et al.^[24] Free-extrusion conditions might be imagined by increasing the layer separation in Figure 2 until the material no longer deposits onto the surface and can be collected by hand. **Table 2** shows the measured birefringence values of freely extruded PLLA at $e_{\text{PLLA}} = 0.01$ and print speeds of $v_p = 1000, 2000, 4000$ and 6000 mm min^{-1} . These reported values are 10 times smaller than those reported for deposited PLLA layer ($L_{\text{PLLA}} = 50 \mu\text{m}$) in Figure 2. A slight increase in measured birefringence is seen with print speed, though the variation measured is significant, which is unsurprising considering the low values of retardation ($\approx 10 \text{ nm}$) measured. These values correspond to the degree of alignment that would be approached if Figure 2 were extended and are a tenth of those shown in this figure. This result suggests that the primary mechanism of alignment is the relative motion between the nozzle and the printing surface.

3.2. Induced Birefringence under Stable Printing Conditions

Increasing the number of layers of material deposited is expected to increase the total retardation of light. To observe birefringence

Table 2. Measured birefringence of freely extruded PLLA.

Print Speed [mm min^{-1}]	Birefringence [$\times 10^{-5}$]	Error [$\times 10^{-5}$]
1000	1.93	0.50
2000	7.23	0.37
4000	2.11	0.17
6000	3.00	1.54

under stable printing, multilayer samples were printed. 3D printed layers produced at layer separations $L_{\text{PLLA}} = 50, 75$ and $100 \mu\text{m}$ and a print speed of $v_p = 6000 \text{ mm min}^{-1}$ are shown in **Figure 4**. On increasing layer number from 2 to 40, retardation was found to increase from 50 to 550 nm. This could be seen clearly when the wedges were placed between crossed polarizing filters, with the direction of printing at 45° to the polarizer (shown in Figure 4b). At $L_{\text{PLLA}} = 50 \mu\text{m}$ (Figure 4bi) the shift in color of transmitted light through the first and into the second order of a Michel Levy chart is clearly seen.

The measured retardation of each layer number is presented in Figure 4c for $L_{\text{PLLA}} = 50, 75,$ and $100 \mu\text{m}$. Retardation can be seen to be independent of layer separation. This satisfies the prediction of presented previously, that induced retardation does not vary with layer separation under the stable printing condition ($h_{\text{PLLA}} = L_{\text{PLLA}}$).

Considering the appearance of the wedges in Figure 4b, a comment might be made on the stability of printing as layer number is increased. A fairly high raster spacing (0.7 mm) was selected to prevent the reheating and disruption of neighboring rasters during deposition. However, individual rasters are not well supported toward the end of a wedge, increasingly so at a higher number of layers where stacked layers may move slightly as the nozzle deposits the next layer of material. This results in the rasters visibly deflecting during printing, which is undesirable for consistent, uniformed and aligned deposition. This instability may contribute to the decreasing gradient of the curve shown for measured retardation with increasing layer number. A progressively less stable stack of layers that moves during depositing may disrupt the aligning effect of the relative motion between the nozzle and print surface. This issue can be resolved by stabilizing the structure using a block geometry where adjacent rasters provide support to one another. This structure is therefore utilized throughout the remainder of this paper.

The calculated birefringence of each raster is shown in Figure 4d. Birefringence is seen to be highest for the lowest layer separation $L_{\text{PLLA}} = 50 \mu\text{m}$. This is not surprising as these results represent an extension of Figure 2 into multilayer stable printing conditions. As samples are printed on a PLLA support layer printed at a slow speed ($L_{\text{PLLA}} = 200 \mu\text{m}$, $e_{\text{PLLA}} = 0.04$, $v_p = 1000 \text{ mm min}^{-1}$) the measured birefringence for a raster in the wedge is expected to be lower than those values reported in Figure 2. This also leads to an increase in birefringence observed between 0 and 10 layers, as material deposited at a faster speed begins to dominate over the slow support layer. On increasing layer number further, birefringence is shown to decrease. The re-heating of printed layers as new material is deposited may contribute to a drop in birefringence through chain relaxation as the PLLA is heated above its glass transition temperature ($T_g = 65 \text{ }^\circ\text{C}$). This effect could be considerable given the variation in alignment through the thickness of a layer predicted in Equation S2 in the Supporting Information. Here, polymer chains might be most aligned at the surface of a layer, and so the overall retardation of a layer is more susceptible to top-down re-heating than if alignment were uniformly distributed. It is important to note that the variation of birefringence within the layer predicted in Equation S2 in the Supporting Information relates to the melt immediately following deposition. As the

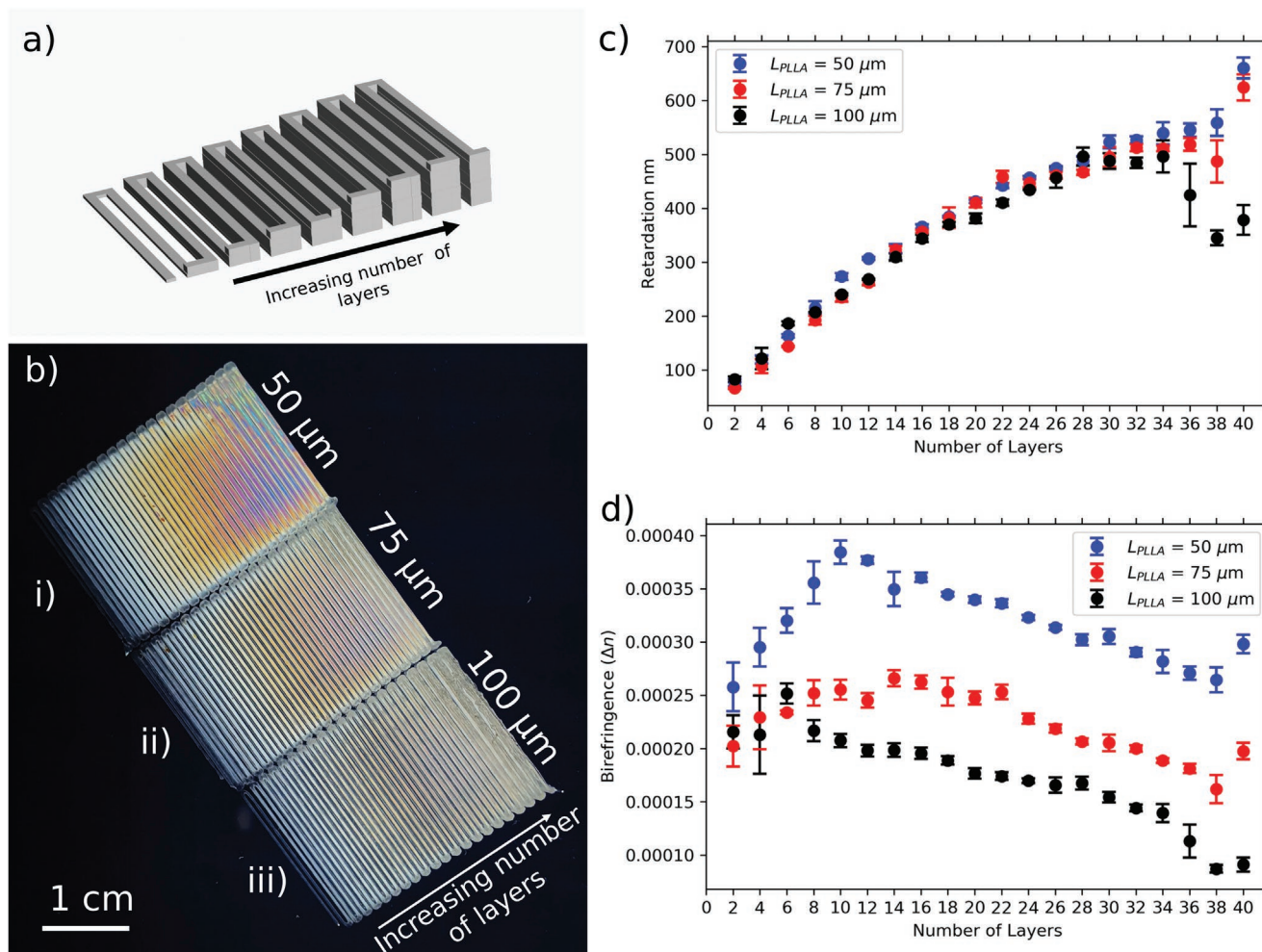


Figure 4. a) A 3D model to demonstrate the sample geometry. b) A series of 3D printed wedges (Layers 2–40, $V_p = 6000 \text{ mm min}^{-1}$, $\epsilon_{\text{PLLA}} = 0.01$) for layer separations $L_{\text{PLLA}} = 50, 75, 100 \mu\text{m}$. c) The measured retardation for each wedge: $L_{\text{PLLA}} = 50 \mu\text{m}$ (blue), $L_{\text{PLLA}} = 75 \mu\text{m}$ (red), $L_{\text{PLLA}} = 100 \mu\text{m}$ (black). d) The calculated birefringence for each raster within the wedges.

polymer takes a finite time to cool through its glass transition there is sufficient time for a reduction in chain alignment. As the bottom surface of a layer is constrained through adhesion, it might be expected that the top surface experience a greater degree of relaxation—as observed in the warping of 3D printed parts.

A reduction in the visibility of transmitted color is apparent as layer separation is increased through $L_{\text{PLLA}} = 50\text{--}100 \mu\text{m}$ (Figure 4bi–biii). The decreasing visibility of the transmitted color might be understood by considering the interface between layers within the printed samples. Figure 5 shows a pictorial representation of the suggested effect of layer separation on interface quality. On decreasing the distance between the nozzle and the print surface whilst maintaining a constant extrusion factor, the pressure and temperature at the interface between the deposited and previous layer are increased. This increases uniformity at the interface by encouraging interdiffusion between layers. Poorly bonded interfaces at higher layer separations lead to increased scattering and reduced transmission of light. This effect has been observed previously by Nelson et al. who report increasing transparency on a reduction

of layer separation ($L = 50 \mu\text{m}$) in their 3D printed microfluidics.^[33] Further, an inset in Figure 5b highlights curvature at the edge of rasters that refracts light on passage through the air-gaps within the 3D print. At higher layer separations this region constitutes a greater portion of the overall structure, owing to the changes in layer cross-section that progress with layer separation.^[34]

A variation in birefringence through the thickness of a printed layer presents an interesting situation at layer interfaces. A refractive index difference at the meeting between the top of one layer and the bottom of the next will lead to a degree of reflection at the interface. This effect will be more pronounced at lower layer separations where the difference between chain alignment at the top and bottom of a layer is expected to be greater.

3.3. Demonstrating Extinction

In Figure 4, it was seen that the deposition of additional layers of printed PLLA lead to an increase in the retardation

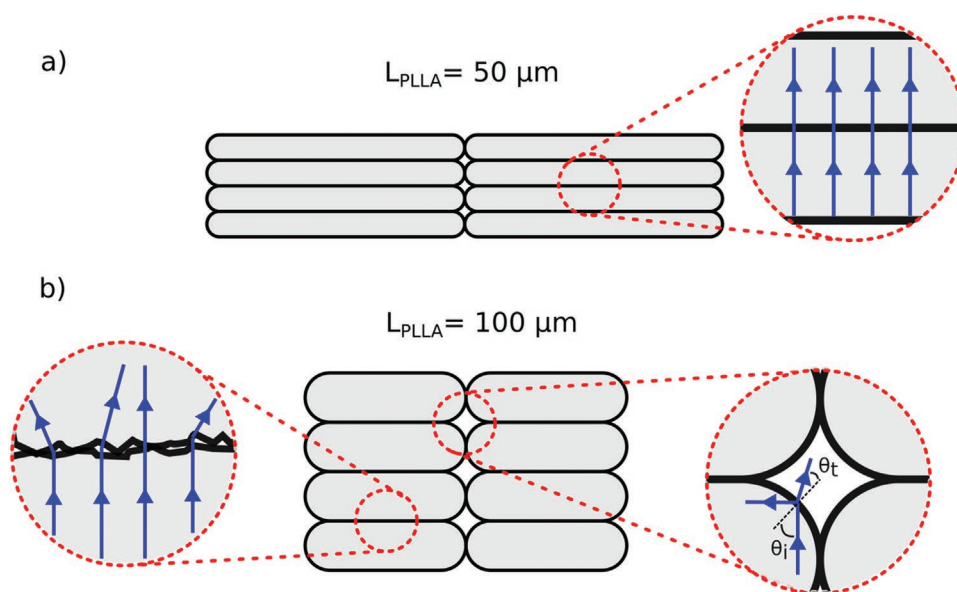


Figure 5. A pictorial representation of the suggested effect of layer separation on the quality of the interface between layers. a) At a low layer separation, $L_{\text{PLLA}} = 50 \mu\text{m}$, transmission of light is reasonably unaffected. b) At higher layer separations, poor interface adhesion leads to an increased scattering of light (inset left) and cross-sectional area changes lead to regions of refraction (inset right) with incoming angle θ_i and outgoing angle θ_t .

of polarized light—an increase in the phase difference experienced by light vibrating in the fast and slow directions propagating through the 3D printed structure. In this situation, light retarded by one layer is further retarded on transmission through the next. A second layer might instead be orientated such that retardation is reduced or eliminated entirely. To demonstrate the extinction of polarized light, through compensation, PLLA layers were printed perpendicularly. In this way, for identical layers the fast axis of one layer is overlaid above the slow axis of another and a result the overall polarization state is unaltered.

A representation of a structure to demonstrate compensation and extinction using induced birefringence is shown in **Figure 6a**. Following a sacrificial PVA ($L_{\text{PVA}} = 200 \mu\text{m}$, $e_{\text{PVA}} = 0.04$, $v_p = 1000 \text{ mm min}^{-1}$), removed after printing, and supporting thicker PLLA layer ($L_{\text{PLLA}} = 200 \mu\text{m}$, $e_{\text{PLLA}} = 0.04$, $v_p = 1000 \text{ mm min}^{-1}$), an 8 layer square was printed in an alternating aligned raster pattern ($L_{\text{PLLA}} = 50 \mu\text{m}$, $e_{\text{PLLA}} = 0.01$, $v_p = 6000 \text{ mm min}^{-1}$), followed by a further PLLA support layer ($L_{\text{PLLA}} = 200 \mu\text{m}$, $e_{\text{PLLA}} = 0.04$, $v_p = 1000 \text{ mm min}^{-1}$) and 8 layer rectangle ($L_{\text{PLLA}} = 50 \mu\text{m}$, $e_{\text{PLLA}} = 0.01$, $v_p = 6000 \text{ mm min}^{-1}$) printed at a perpendicular orientation. In this way, half of the test sample is covered with an equal number of perpendicular layers. A photograph of the printed structure is shown in **Figure 6b** with arrows overlaid to indicate the direction of printing.

The sample was imaged between crossed polarizing filters with printing directions orientated at 0° (**Figure 6c**) and 45° degrees (**Figure 6d**) to the direction of polarization. In **Figure 6c**, where alignment within layers is aligned with the axis of the polarizer or analyzer, only scattering of light from layer and raster interfaces is visible. In **Figure 6d**, the birefringence of printed layers is clearly visible. Light is transmitted through the uncovered region A. In the covered region, B, extinction can be seen where layers overlap and the net phase difference between

light vibrating along fast and slow directions is zero. Scattering from layer and raster interfaces can also be seen.

3.4. 3D Printing of a Michel-Levy Chart

The control that print speed has over induced birefringence can be clearly demonstrated in the printing of a Michel-Levy chart. As seen in **Figure 4**, many layers of PLLA are required to produce significant color at print speeds a standard 3D printer is capable of achieving ($<10000 \text{ mm min}^{-1}$). To make a sample capable of producing colors throughout the first order of a Michel-Levy chart, a 40 layer PLLA block was printed ($L_{\text{PLLA}} = 50 \mu\text{m}$, $e_{\text{PLLA}} = 0.01$) onto a thicker PLLA supporting layer ($L_{\text{PLLA}} = 200 \mu\text{m}$, $e_{\text{PLLA}} = 0.04$, $v_p = 1000 \text{ mm min}^{-1}$), and removable sacrificial layer of PVA ($L_{\text{PVA}} = 200 \mu\text{m}$, $e_{\text{PVA}} = 0.04$, $v_p = 1000 \text{ mm min}^{-1}$). Layers were deposited in an alternating aligned raster pattern, with print speed increasing between pairs of adjacent rasters such that there are two printed lines for each print speed. A 3D model of this printing pattern can be seen in **Figure 7a**. Print speed was progressively increased from $v_p = 500 \text{ mm min}^{-1}$ to $v_p = 9000 \text{ mm min}^{-1}$.

The transmission of colors throughout the first, and part of the second order of a Michel-Levy chart are visible in **Figure 7b**, where the sample is imaged at 45° between a crossed polarizer and analyzer. At the lowest speed, 500 mm min^{-1} , the rasters appear white corresponding to around 100 nm of retardation. As speed is increased to 9000 mm min^{-1} , sample retardation increases to almost 800 nm , corresponding to a green appearance. Retardation is shown to vary across the length of rasters, reaching a maximum in their centres. This is due to the acceleration of the nozzle as it reaches the target printing speed. A plot of the retardation values measured at the centre of rasters at each print speed is shown in **Figure 7c**.

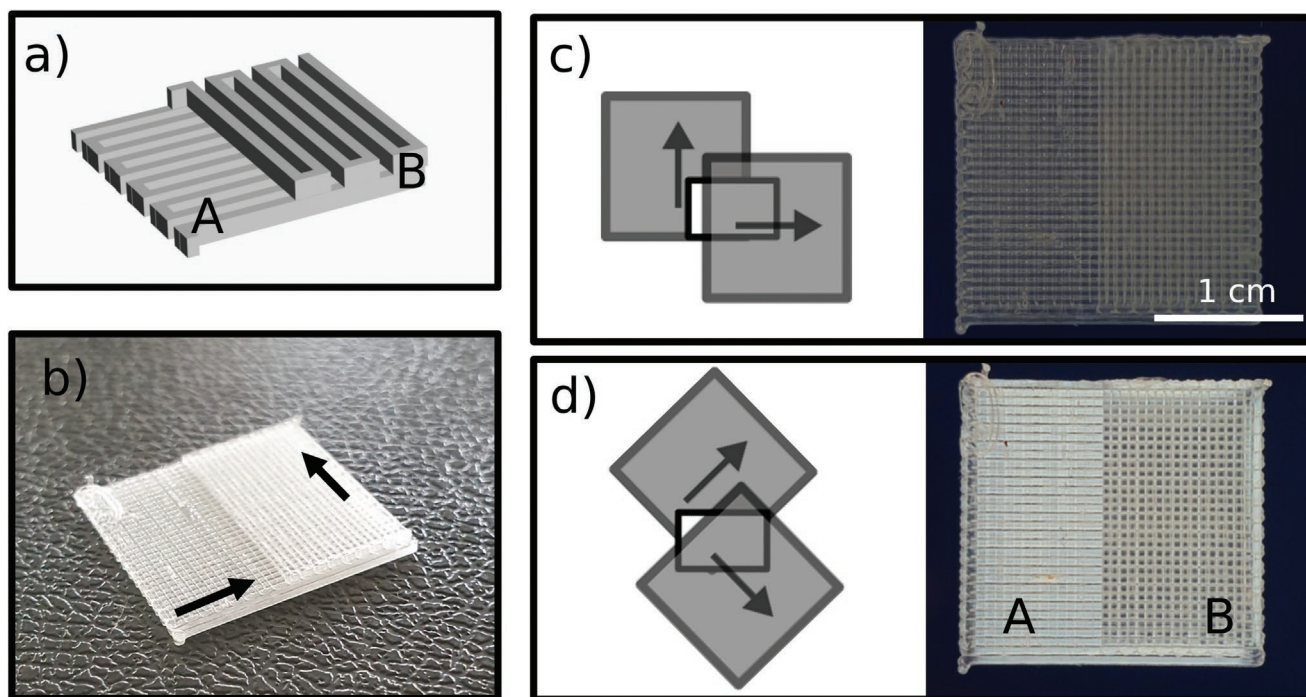


Figure 6. a) A 3D model to demonstrate the sample geometry and printing direction. b) A photograph of a 3D printed structure consisting of an 8 layer square ($L_{\text{PLLA}} = 50 \mu\text{m}$, $e_{\text{PLLA}} = 0.01$, $v_p = 6000 \text{ mm min}^{-1}$) with half of its surface area covered by an 8 layer rectangle ($L_{\text{PLLA}} = 50 \mu\text{m}$, $e_{\text{PLLA}} = 0.01$, $v_p = 6000 \text{ mm min}^{-1}$) printed at a 90° rotation (Arrows indicate the printing direction). c) Sample placed at 0° between an analyzer and polarizer. Increased scattering can be seen in the covered region, but at minimal level overall if any retardation of light is observed. d) Sample placed at 45° between an analyzer and polarizer. Retardation of light is observed in the uncovered region, with extinction seen where perpendicular layers overlap in the covered region.

In modeling the induced birefringence during 3D printing, an exponential approach to a maximum retardation was proposed

$$\Gamma = \Gamma_{\text{max}} (1 - \exp(-\Omega)) \quad (5)$$

A curve of this form is fitted in Figure 7d where $\Gamma_{\text{max}} = 800 \text{ nm}$ and $\Omega = 0.00035 v_p$. The transmitted colors expected on ideal transmission of a uniform spectrum of light were calculated and are displayed underneath the respective fitted retardation values shown in Figure 7d. These modeled colors are in agreement with those observed in practice in Figure 7c. These values highlight a measured proportionality between Ω and v_p as predicted previously in Equation S2 in the Supporting Information through the modeling of strain rate during deposition.

For non-zero print speeds some degree of alignment is likely to be present. This is especially noticeable at higher numbers of layers where even relatively slow print speeds (such as 500 mm min^{-1} in Figure 7c) produce noticeable transmission between when observed between crossed polarising filters. The extinction demonstrated in Figure 6 through the printing of perpendicular layers can be used to print a Michel-Levy chart that includes regions of little to no retardation. The variable speed block shown in Figure 7a was next printed with an additional perpendicular support PLLA layer ($L_{\text{PLLA}} = 200 \mu\text{m}$, $e_{\text{PVA}} = 0.04$, $v_p = 1000 \text{ mm min}^{-1}$) and compensating wedge ($L_{\text{PLLA}} = 50 \mu\text{m}$, $e_{\text{PLLA}} = 0.01$, $v_p = 6000 \text{ mm min}^{-1}$) varying from 2 to 20 layers. This structure is modeled in

Figure 8a and pictured in Figure 8b. In this way, the number of compensating layers required to achieve extinction of a given print speed could be determined. When the sample is viewed through a crossed analyzer and polarizer, with the printing direction aligned to the polarizer there is no discernable difference between rasters (Figure 8c). With the sample orientated such that the print direction is at 45° , variation with print speed is clear. A reduction in retardation is seen where perpendicular layers meet. Rasters within this structure can be referenced with the i and j coordinates labeled in Figure 8d. Moving through i , print speed is increased leading to an increase in retardation. On moving through j , the number of compensating layers is increased, reducing retardation. At $v_p = 500 \text{ mm min}^{-1}$, 6 layers of PLLA ($L_{\text{PLLA}} = 50 \mu\text{m}$, $e_{\text{PLLA}} = 0.01$, $v_p = 6000 \text{ mm min}^{-1}$) are sufficient to achieve extinction (circled in Figure 8d).

3.5. Steganography with Induced Birefringence

Induced alignment may be harnessed to introduce a new type of 3D printed steganography. Figure 9 shows a 3D rendering of a steganographic print viewed between crossed polarizers, orientated to achieve maximum transmission (print direction at 45° to polarizing direction). By varying printing speed across a layer a spatial variation in polymer chain alignment, and induced birefringence, can be achieved. In this way, an image, the acronym "CCMM" for the Cambridge Centre of Medical Materials, can be concealed within the bulk of a 3D

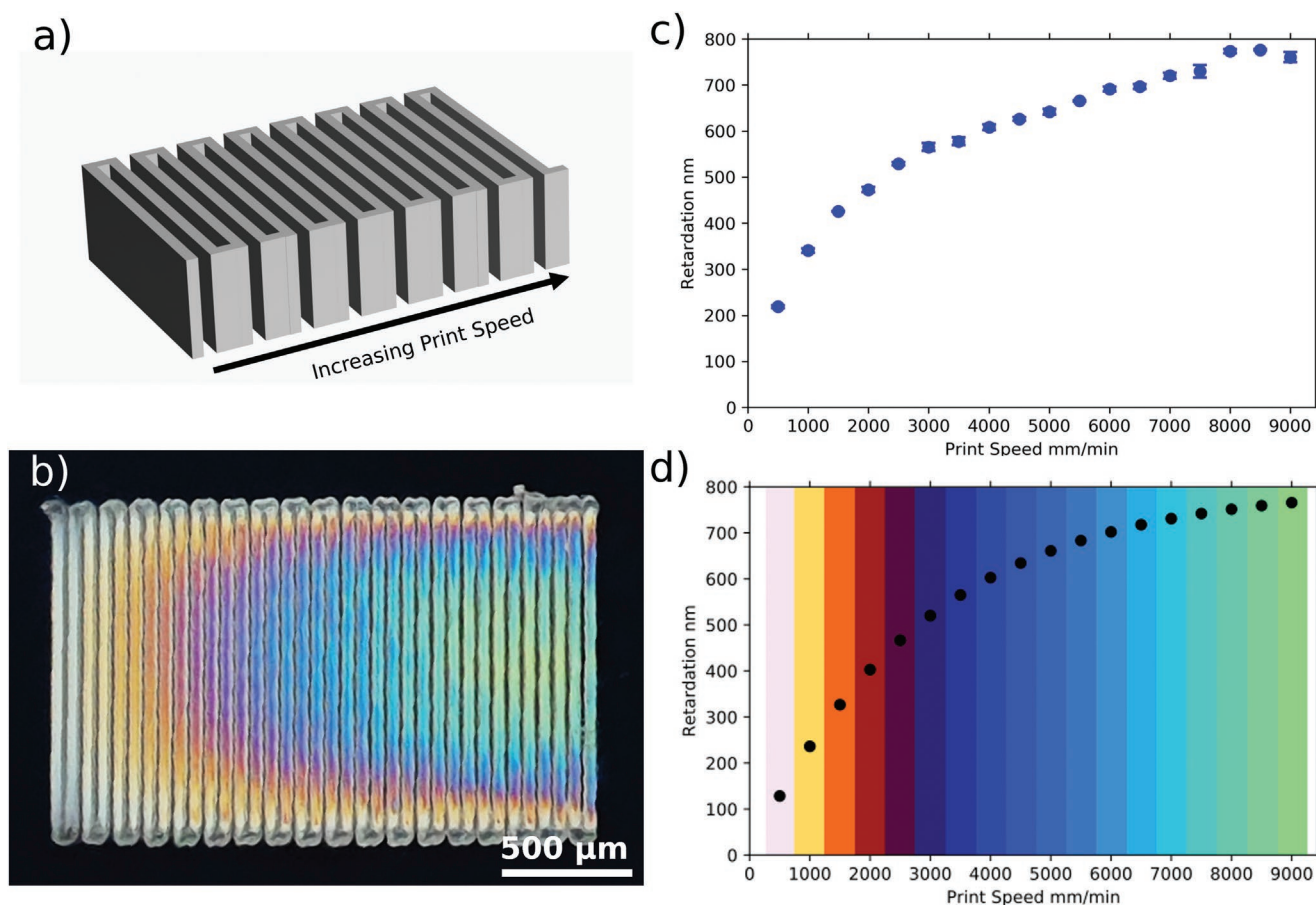


Figure 7. a) A 3D model to show the sample geometry. b) Sample placed at 45° and imaged between a crossed analyzer and polarizer. c) Measured retardation for each print speed with the block. d) an exponential fit for the variation of retardation with print speed of the form $\Gamma = \Gamma_{\max} (1 - \exp(-A\nu_p))$, where $\Gamma_{\max} = 800$ nm and $A = 0.00035$. A predicted transmitted color for an incident white light spectrum is overlaid.

printed block. The induced molecular alignment is shown in Figure 9, with a small region representing part of the letter “C” inspected. Printing speed is low for the black regions (low retardation leading to limited transmission of light) and high in the white region (higher retardation leading to transmission of white light).

Steganographic prints were prepared through a combination of the techniques discussed in this article. A removable bed-levelling sacrificial PVA layer was first deposited ($L_{\text{PVA}} = 200$ μm, $e_{\text{PVA}} = 0.04$, $\nu_p = 1000$ mm min⁻¹) followed by a supporting PLLA layer ($L_{\text{PLLA}} = 200$ μm, $e_{\text{PLLA}} = 0.04$, $\nu_p = 1000$ mm min⁻¹). Images may then be stored as changes in retardation by spatially alternating print speed within a 40 layer PLLA block with an alternating raster pattern ($L_{\text{PLLA}} = 50$ μm, $e_{\text{PLLA}} = 0.01$). Finally a second PLLA support layer ($L_{\text{PLLA}} = 200$ μm, $e_{\text{PLLA}} = 0.04$, $\nu_p = 1000$ mm min⁻¹) and compensating 6 layer pattern ($L_{\text{PLLA}} = 50$ μm, $e_{\text{PVA}} = 0.01$, $\nu_p = 6000$ mm min⁻¹) are deposited at 90° to allow the printing of regions of low retardation. For forming “CCMM,” text is printed at $\nu_p = 6000$ mm min⁻¹, with surrounding regions at $\nu_p = 1500$ mm min⁻¹. An exploded view model of the printed structure can be seen in Figure 10.

The steganographic print conceptualised in Figure 9 is fabricated in Figure 11. A photograph of the 3D printed block can be seen in Figure 11a. The block appears uniform, with

consistent layers, and the text is not visible to the naked eye. When viewed between cross polarising filters, the induced birefringence becomes apparent. In Figure 11b, with printing direction aligned with the polarising direction, minimal effect can be seen. At 45° alignment, the logo “CCMM” becomes visible as orange/red text on a light background, corresponding to retardations of around 450 nm and 150 nm respectively (Figure 11c).

More complex steganographic prints can be formed using a wider range of print speeds. In Figure 12a a multicolored cartoon character was stored, using $\nu_p = 500, 750, 1000, 2000,$ and 6000 mm min⁻¹ to produce black, grey, white, skin tone, and red respectively. The cartoon character, is revealed in Figure 12b where the print is viewed between crossed polarizing filters at a 45° angle. Some presence of the modification is visible in Figure 12a at the transition regions between printing speeds. This small effect is caused by a delay in the extrusion of material from the nozzle as the print bed initially accelerates which results in a lower deposition than is expected. This effect is significantly less pronounced in Figure 11a where the differences in print speed, and hence acceleration, are less drastic. Likewise, no difference can be seen in the dimensions of rasters printed at contrasting print speeds, 500 and 9000 mm min⁻¹ in Figure 7. The offset in extrusion response with bed acceleration can be accounted with a graduated extrusion factor at the

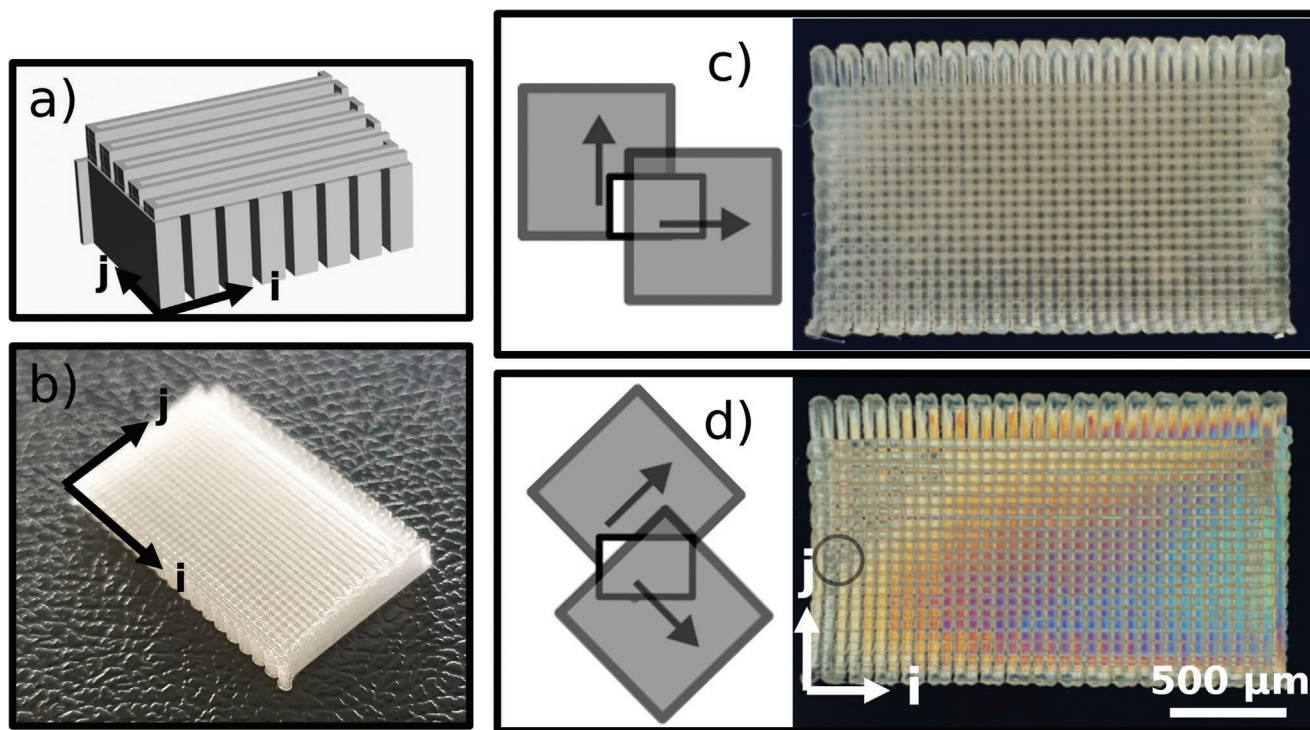


Figure 8. A 3D printed Michel-Lévy chart consisting of a 40 layer block ($L_{\text{PLLA}} = 50 \mu\text{m}$, $e_{\text{PLLA}} = 0.01$) printed at a uniform print direction, at incrementally increasing target speeds between 500 and 9000 mm min^{-1} , and a wedge (2–20 layers) with a perpendicular printing direction ($L_{\text{PLLA}} = 50 \mu\text{m}$, $e_{\text{PLLA}} = 0.01$, $V_p = 6000 \text{ mm min}^{-1}$). a) A 3D model highlighting sample geometry. b) Photographs of the printed chart. c) Chart placed at 0° between an analyzer and polarizer: uniform scattering of light. d) Chart placed at 45° between an analyzer and polarizer: A range of retardations is revealed spanning the full first, and half of the second order.

start and end of speed transitions. Nevertheless, the specific transmission colors and exact spectral response of 3D printed regions provide sufficient combinations to encode information, with the number of potential values at each location limited only by the ability to detect sufficient differences in retardation.

3.6. Material Selection, Challenges, and Limitations

In generalizing this technique to other materials and 3D printers it is important to address and overcome some existing limitations in the process. Fundamentally, this technique has only been demonstrated through this paper for a specific PLLA filament, and must be explored and implemented further with other transparent polymers if it is to gain widespread adoption. The recent introduction of commercial available transparent PLA filament (Prusa, Natureworks 4043D PLLA) might serve as a good candidate. In general, a candidate polymer should be transparent and typically amorphous after printing. This presently excludes the overwhelming majority of 3D printed structures which often feature opaque filler materials to provide a colored appearance. However, for most applications which utilize PLLA a switch to a transparent filament would be perfectly acceptable, as colored fillers are merely cosmetic additives. Materials such as clear polycarbonate, PETG (polyethylene terephthalate glycol) and clear ABS might be considered as trial candidates. Nevertheless, this technique might be

explored in the future to utilize wavelengths of light outside the visible range, to implement 3D printing steganography in opaque colored materials. Likewise, an investigation into the effects of glass transition and molecular weight on alignment would be beneficial, as these are expected to be influential. From a hardware perspective, access to higher quality printers will enable improvements to this process. For example, the pixel resolution shown in Figures 11 and 12 is limited to 0.5 mm—increased nozzle acceleration would allow print speeds to be changed over shorter distances, and increase the complexity of spatial variation that might be achieved. Likewise, increasing print stability and consistency achieved through the use of higher quality printers will allow reduction in error

4. Conclusion

This paper offers a demonstration of the potential for point-by-point material property control through fused deposition modeling. We have presented a simple model by which to understand the effects of extrusion factor, printing speed, layer separation, and nozzle and filament diameters on induced molecular alignment in 3D printed PLLA. The interaction of aligned polymer chains with light has been investigated through measuring the birefringence of 3D printed layers. Birefringence in single layers was shown to increase with both increasing print speed and reducing layer separation. The cumulative retardation of

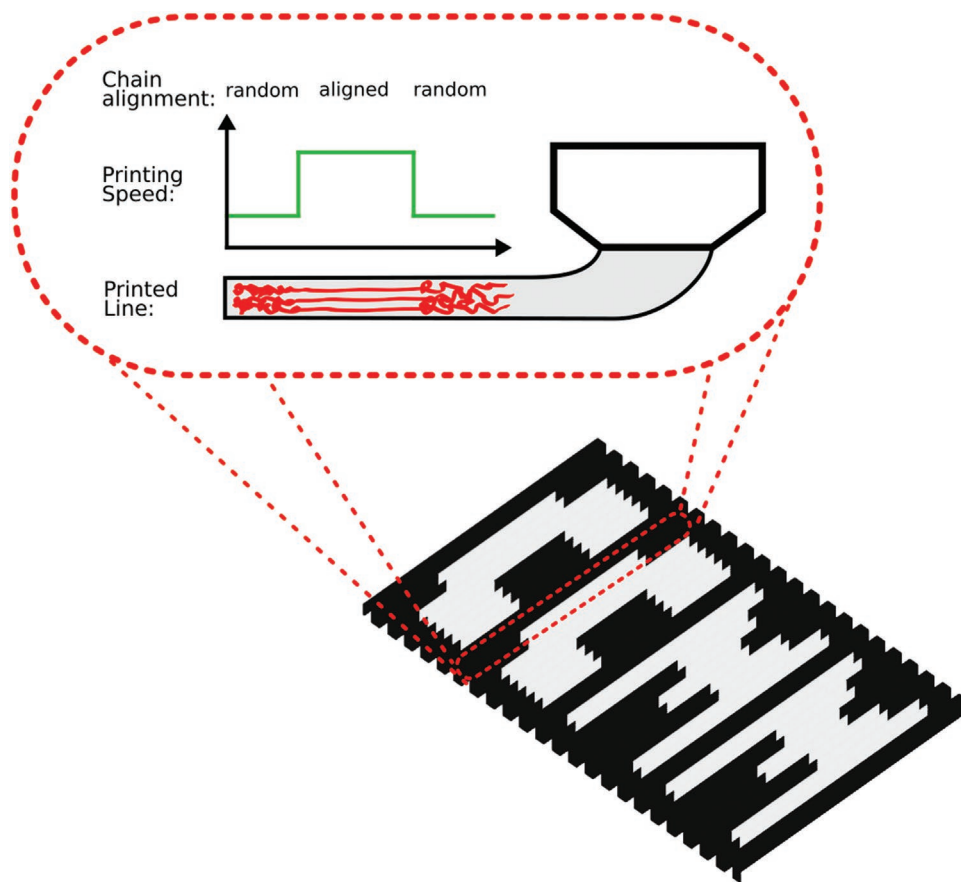


Figure 9. A schematic to highlight the variation in polymer chain alignment throughout a layer printed with a spatially varying print speed. Text, “CCMM,” is concealed unless observed using polarizers.

multiple layers of printed PLLA has been utilized to demonstrate extinction and elicit a wide range of color transmissions cumulating in the 3D printing of a Michel-Levy chart. Finally,

the spatial variation of induced molecular alignment and birefringence has been used to 3D print multicolor steganographic prints. The results presented are significant in demonstrating

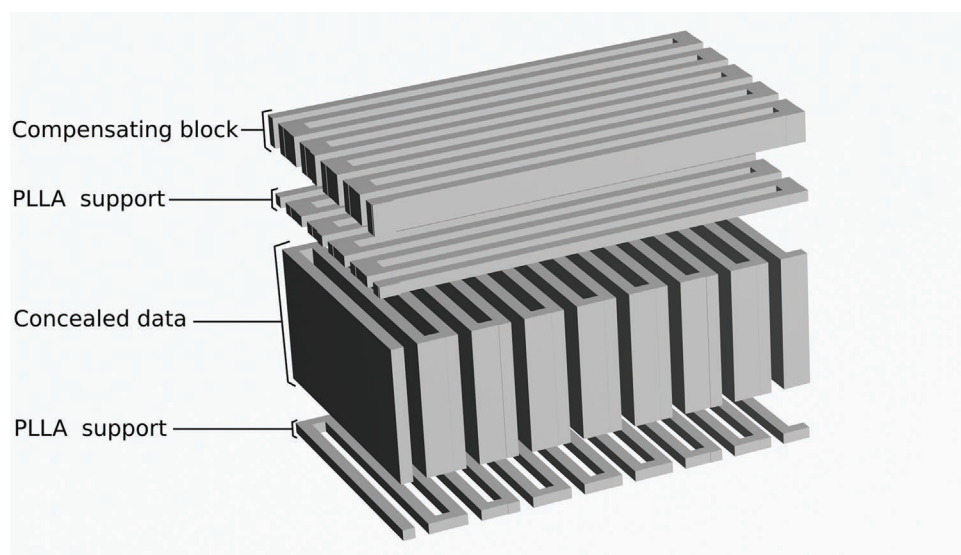


Figure 10. A model showing an exploded view of a steganographic print.

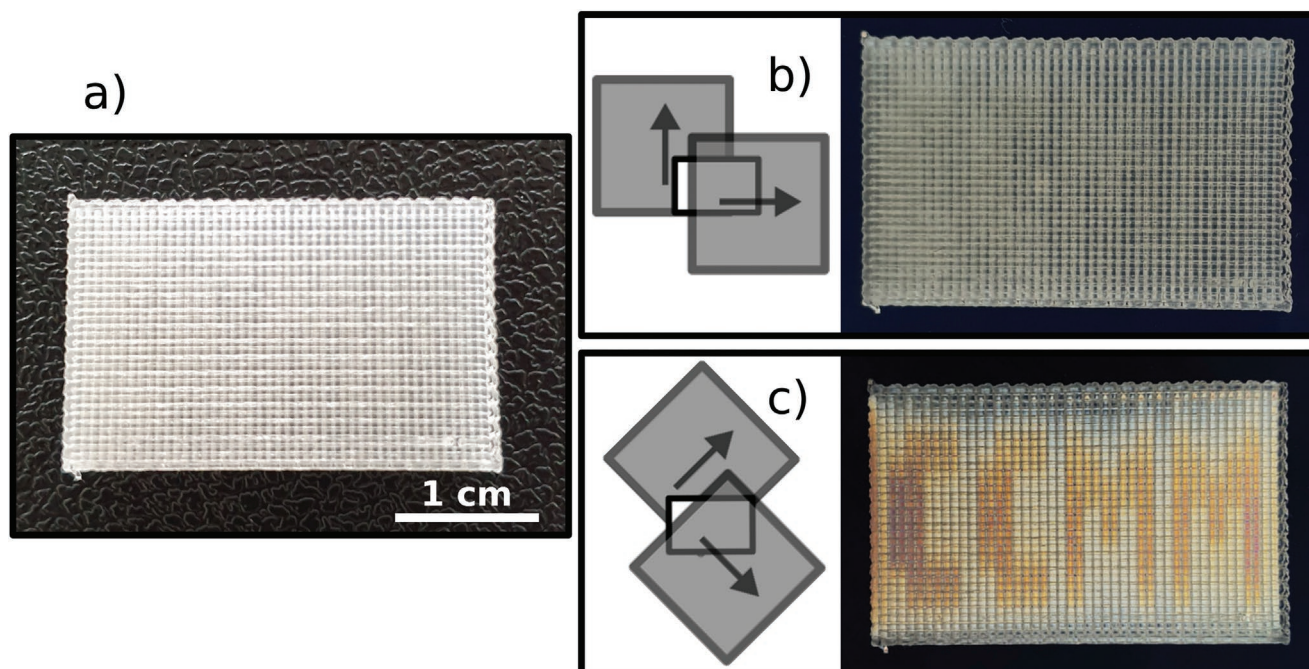


Figure 11. a) 3D printed block ($L_{\text{PLLA}} = 50 \mu\text{m}$, $e_{\text{PLLA}} = 0.01$). b) Sample placed at 0° between an analyzer and polarizer—image appears uniform. c) Sample placed at 45° between an analyzer and polarizer: an orange/red “CCMM” on a white background is revealed, corresponding to retardations of 450 nm and 150 nm respectively.

within-layer property variation in 3D printing. Spatially controlled molecular alignment might find application in the 3D printing of photonic devices, allowing both the embedding of waveguiding structures within bulk prints, or enabling rapid production of thin optically active layers. Further, spatial variation of material properties, such as birefringence, may prove useful for part identification and tracking, printer fingerprinting, and the 3D printing of unique identification objects such as access cards.

5. Experimental Section

3D Printer and Materials: Samples were produced on a self-assembled 3D printer (Prusa MK2S, measured nozzle diameter = $398 \mu\text{m}$) that has been retrofitted with a Titan extruder (E3D), providing a reduced 3:1 gear ratio to increase extrusion torque. Extrusion was calibrated according to the standard practice of adjusting the motor step rate to ensure accurate feed rates. Extrusion and bed temperatures, T_{ext} and T_{bed} , were set to $215^\circ\text{C}/55^\circ\text{C}$ and $195^\circ\text{C}/55^\circ\text{C}$ for PLLA and PVA filaments respectively. The printer stage acceleration was limited to 1500 mm s^{-2} , and print speeds between 500 and 9000 mm min^{-1} were

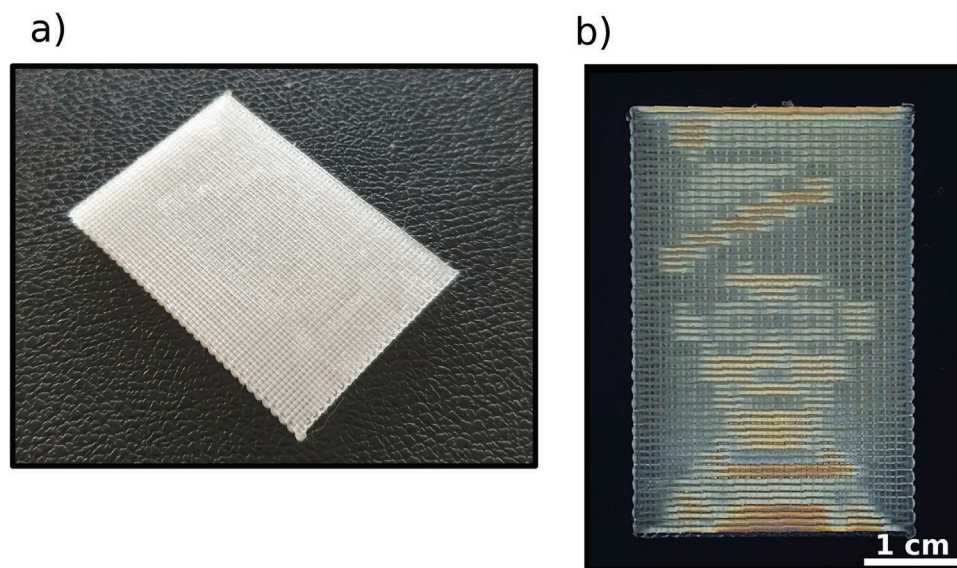


Figure 12. a) 3D printed block ($L_{\text{PLLA}} = 50 \mu\text{m}$, $e_{\text{PLLA}} = 0.01$). b) Sample placed at 45° degrees between an analyzer and polarizer: a multicolor cartoon character is revealed.

verified by timing 200 mm travel distances. Printing was managed by usb tether to a computer running a Pronterface controller, allowing the direct execution of custom Gcode scripts. Gcode files were prepared in MATLAB with functions written to output Gcode in the flavor required for the Prusa MK2S. Defined printing moves, speeds and extrusion factors were converted to Gcode—with new absolute motor positions of the printer calculated based on the tracked position within the script. The horizontal displacement of the nozzle was calculated such that the extruder motor was turned to eject material according to the extrusion factor condition (e = length of filament extruded/horizontal nozzle displacement).

Two feedstock polymers were used in this study. Samples were printed from PLLA filament, Ingeo Biopolymer 2500HP (Natureworks) that had been extruded into approximately 40 cm lengths using a Noztek Pro Extruder (182 °C at a target filament diameter of 1.75 mm). Extruded filament mean diameters were measured to be between 1.60 and 1.70 mm, with those outside of this range excluded from use. A tolerance of 0.05 mm deviation from the mean diameter along the length of the filament was deemed acceptable – failing filaments were discarded. Extrusion factors (e_{PLLA}) were scaled with respect to a 1.75 mm filament diameter to maintain a constant volume of extrusion between prints. Support layers were printed using PrimaSelect PVA+ Soluble Support filament (1.75 mm diameter) purchased from Prusa Research (Czech Republic). Before printing, the PVA filament was vacuum dried overnight.

Printing Samples: All samples were printed on a PVA sacrificial layer of $L_{\text{PVA}} = 200 \mu\text{m}$, $e_{\text{PVA}} = 0.04$, $v_p = 1000 \text{ mm min}^{-1}$ to aid sample removal and first layer print-to-print consistency.^[25] This layer was removed by peeling. The inclusion of a low speed, thicker PLLA layer ($L_{\text{PLLA}} = 200 \mu\text{m}$, $e_{\text{PLLA}} = 0.04$, $v_p = 1000 \text{ mm min}^{-1}$) was necessary to provide a base for all structures in this article onto which to consistently deposit thinner layers at high speed.

Modeling Transmitted Color: MATLAB was used to calculate the expected color of transmitted light through 3D printed samples. The basic functionality of the model follows the description laid out by Sørensen in their first principle calculation of a Michel-Lévy chart.^[35] In this paper, an empirical model of the variation of retardation with print speed is substituted in the place of the linearly increasing retardation values typically used to form a Michel-Lévy chart.

Characterization: The birefringence of printed samples was viewed and photographed using a white light illuminator with an analyzer and polarizer cut from a linear polarizing sheet. Sample retardation was measured by two methods. Transmitted color was compared with a calculated Michel-Lévy chart to find retardations. For more accurate measurements, retardation was found using a Polarising Petrological microscope (Swift) and an inserted Ehringhaus compensator (Zeiss)—with tilt angles referenced to retardation values using a look up table supplied by the manufacturer. Sample thicknesses were measured through cross-sectional optical microscopy as previously reported^[25], where on inspection, sample cross-sectionals were found to be flat with curved edges. Surface deviations were negligible in comparison to the sample-to-sample variation in printed layer thickness ($\approx 10\%$).

Statistical Analysis: During characterization, measured properties are presented as mean values with experimental error reported as standard deviation. In exploring the effect of layer separation and print speeds in Figures 2 and 8 samples are considered for each printing condition. For investigated the effect of extrusion factor on induced birefringence in Figures 3 and 7 samples were selected for each printing speed, each corresponding to a different extrusion factor between 0.01 and 0.05. Retardation values were measured within single layers at three equidistance points across sample lengths. Errors were appropriately combined for the calculation of birefringence.

Supporting Information

Supporting Information is available from the Wiley Online Library or from the author.

Conflict of Interest

The authors declare no conflict of interest.

Data Availability Statement

The data that support the findings of this study are openly available in Apollo at <https://doi.org/10.17863/CAM.82239>, reference number 82239.

Keywords

3D printing, alignment, birefringence, FFF, steganography

Received: January 25, 2022

Revised: March 29, 2022

Published online:

- [1] M. Zarek, M. Layani, I. Cooperstein, E. Sachyani, D. Cohn, S. Magdassi, *Adv. Mater.* **2016**, *28*, 4449.
- [2] Q. Ge, H. J. Qi, M. L. Dunn, *Appl. Phys. Lett.* **2013**, *103*, 131901.
- [3] Q. Ge, C. K. Dunn, H. J. Qi, M. L. Dunn, *Smart Mater. Struct.* **2014**, *23*, 094007.
- [4] J. Wu, C. Yuan, Z. Ding, M. Isakov, Y. Mao, T. Wang, M. L. Dunn, H. J. Qi, *Sci. Rep.* **2016**, *6*, 24224.
- [5] Y. Mao, K. Yu, M. S. Isakov, J. Wu, M. L. Dunn, H. Jerry Qi, *Sci. Rep.* **2015**, *5*, 13616.
- [6] G. C. Adhikari, S. Thapa, H. Zhu, P. Zhu, *Adv. Opt. Mater.* **2019**, *7*, 1900916.
- [7] Y. L. Kong, I. A. Tamargo, H. Kim, B. N. Johnson, M. K. Gupta, T. -W. Koh, H.-A. Chin, D. A. Steingart, B. P. Rand, M. C. Mcalpine, *Nano Lett.* **2014**, *14*, 7017.
- [8] C.-L. Tai, W.-L. Hong, Y.-T. Kuo, C.-Y. Chang, M.-C. Niu, M. Karupathevar Ponnusamythevar Ochathevar, C.-L. Hsu, S.-F. Horng, Y.-C. Chao, *ACS Appl. Mater. Interfaces* **2019**, *11*, 30176.
- [9] S.-U. Zhang, *Appl. Sci.* **2018**, *8*, 1224
- [10] J. Skowrya, K. Pietrzak, M. A. Alhnan, *Eur. J. Pharm. Sci.* **2015**, *68*, 11.
- [11] M. Sadiá, A. Sośnicka, B. Arfat, A. Isreb, W. Ahmed, A. Kelarakis, M. A. Alhnan, *Int. J. Pharm.* **2016**, *513*, 659,
- [12] H. Kadry, T. A. Al-Hilal, A. Keshavarz, F. Alam, C. Xu, A. Joy, F. Ahsan, *Int. J. Pharm.* **2018**, *544*, 285,
- [13] K. Willis, E. Brockmeyer, S. Hudson, I. Poupyrev, in *Proc. of the 25th Annual ACM Symp. on User Interface Software and Technology* **2012**, pp. 589–598, <https://doi.org/10.1145/2380116.2380190>.
- [14] N. Vaidya, O. Solgaard, *Microsyst. Nanoeng.* **2018**, *4*, 18.
- [15] H. Gao, G. F. R. Chen, P. Xing, J. W. Choi, H. Y. Low, D. T. H. Tan, *Adv. Opt. Mater.* **2020**, *8*, 2000613.
- [16] K. Weber, D. Werdehausen, P. König, S. Thiele, M. Schmid, M. Decker, P. W. De Oliveira, A. Herkommer, H. Giessen, *Opt. Mater. Express* **2020**, *10*, 2345.
- [17] S. Nocentini, D. Martella, C. Parmeggiani, D. S. Wiersma, *Adv. Opt. Mater.* **2019**, *7*, 1900156.
- [18] E. Nseowo Udofia, W. Zhou, *Addit. Manuf.* **2020**, *31*, 100912.
- [19] S. T. Parker, P. Domachuk, J. Amsden, J. Bressner, J. A. Lewis, D. L. Kaplan, F. G. Omenetto, *Adv. Mater.* **2009**, *21*, 2411.
- [20] S. Nizamoglu, M. C. Gather, M. Humar, M. Choi, S. Kim, K. S. Kim, S. K. Hahn, G. Scarcelli, M. Randolph, R. W. Redmond, S. H. Yun, *Nat. Commun.* **2016**, *7*, ncomms10374.
- [21] S. A. Ghodbane, N. S. Murthy, M. G. Dunn, J. Kohn, *Biofabrication* **2019**, *11*, 045004.
- [22] E. N. Udofia, W. Zhou, *J. Manuf. Sci. Eng.* **2019**, *141*, 050801.
- [23] L. Landau, B. Levich, in *Dynamics of Curved Fronts* (Ed: P. Pelcé), Academic Press, Amsterdam **1988**, pp. 141–153.

- [24] N. M. Hassan, K. B. Migler, A. R. Hight Walker, A. P. Kotula, J. E. Seppala, *MRS Commun.* **2021**, *11*, 157.
- [25] D. M. Roper, K.-A. Kwon, S. M. Best, R. E. Cameron, *Appl. Sci.* **2021**, *11*, 6320.
- [26] F. D'elia, F. Pisani, A. Tredicucci, D. Pisignano, A. Camposeo, *Adv. Mater. Technol.* **2022**, *7*, 2101129.
- [27] A. E. Likhtman, in *Polymer Science: A Comprehensive Reference* (Eds: K. Matyjaszewski, M. Möller), Elsevier, Amsterdam **2012**, pp. 133–179.
- [28] J. Gao, J. H. Weiner, *Macromolecules* **1992**, *25*, 3462.
- [29] W. Zhang, J. Chen, H. Zeng, in *Polymer Science and Nanotechnology* (Ed: R. Narain), Elsevier, Amsterdam **2020**, pp. 149–178.
- [30] A. Keller, H. W. H. Kolnaar, in *Materials Science and Technology* (Eds: R. W. Cahn, P. Haasen, E. J. Kramer), Wiley-VCH Verlag GmbH & Co. KGaA, Weinheim, Germany **2006**, p. mst0210.
- [31] W. Michaeli, M. Koschmieder, in *Comprehensive Composite Materials* (Eds: A. Kelly, C. Zweben), Pergamon, Oxford **2000**, pp. 853–872.
- [32] G. L. Wilkes, *J. Chem. Educ.* **1981**, *58*, 880
- [33] M. D. Nelson, N. Ramkumar, B. K. Gale, *J. Micromech. Microeng.* **2019**, *29*, 095010.
- [34] M. P. Serdeczny, R. Comminal, D. B. Pedersen, J. Spangenberg, *Addit. Manuf.* **2018**, *24*, 145.
- [35] B. E. Sørensen, *Eur. J. Mineral.* **2013**, *25*, 5.